ORIGINAL ARTICLE

Mechanochemical synthesis of nanophotocatalysts SiO$_2$/TiO$_2$/Fe$_2$O$_3$: their structural, thermal and photocatalytic properties

Karolina Kucio[1] · **Barbara Charmas[1]** · **Sylwia Pasieczna-Patkowska[1]** · **Magdalena Zięzio[1]**

Abstract

In the study the mechanochemical synthesis was used to prepare photocatalytic materials based on TiO$_2$, SiO$_2$, and Fe$_2$O$_3$. During the preparation the impact of composition, milling speed, and calcination process on the properties of the composites was investigated. The structural and thermal properties of photocatalysts were determined using the N$_2$ adsorption/desorption, XRD, and FT-IR/PAS methods. The thermal stability of the obtained materials was also examined (TG/DTG). Moreover, their photocatalytic activity was tested in relation to Methylene Blue at UV and Vis radiation. The results indicate that the mechanochemical synthesis in the high-energy planetary mill is an effective method for obtaining materials with photocatalytic properties at the UV and Vis radiation. It was shown that the removal process of MB may be described by the pseudo-first-order kinetics.

Keywords Photocatalysts · Photocatalysis · Mechanochemical synthesis · TiO$_2$ · Nanomaterials · Methylene blue degradation

Introduction

In recent years an intensive increase in global environmental pollution has been observed. It is caused by an increase in consumption and intensive industrial development. For the general environmental protection regulations have been developed to followed when designing technological processes and in many other aspects of human activity (Anastas and Kirchhoff 2002). Among such environmentally friendly methods, wastewater and groundwater treatment processes, which are essential in clean and sustainable water production technologies, are of particular importance. Due to the high cost and depletion of global resources of natural waters, purifying water from various types of contamination is a fundamental problem (Baoum et al. 2019).

One type of pollution are dyes, unsaturated aromatic chemical compounds characterized by e.g.: colour, solubility, durability, toxicity and very low ability to natural degradation (Julkapli et al. 2014). During wastewater treatment different purification methods can be applied. These are: physical (filtration, sedimentation or segregation), physicochemical (coagulation, chemical oxidation, adsorption or ion exchange), and biological (anaerobic and aerobic treatment) methods (Santhi et al. 2015). Many of them are not advantageous for the environment, ineffective, time and cost consuming and often result in dangerous and toxic by-products formation.

Nowadays photocatalytic oxidation processes, as a low-cost and environmentally friendly procedure, show great potential for organic dyes removal from water (Mohamed et al. 2013; Sin et al. 2012; Pirkanniemi and Sillanpää 2002). One of the most frequently used and effective photocatalysts is TiO$_2$ (Khaki et al. 2018; Ahmadpour et al. 2018). This substance is easily available, relatively cheap, non-toxic, and safe for people and the environment (Zaleska 2008; Leong et al. 2014). It is very important that TiO$_2$ exhibits also the antibacterial properties (Trapalis et al. 2003). This semiconductor has a wide bandgap 3.2 eV for anatase and 3.0 eV for

✉ Karolina Kucio
  karolina.kucio@poczta.umcs.lublin.pl

  Barbara Charmas
  barbara.charmas@poczta.umcs.lublin.pl

  Sylwia Pasieczna-Patkowska
  sylwia.pasieczna@poczta.umcs.lublin.pl

  Magdalena Zięzio
  magdalena.ziezio@poczta.umcs.lublin.pl

1   Institute of Chemical Sciences, Faculty of Chemistry, Maria Curie-Sklodowska University, Maria Curie-Sklodowska Sq. 3, 20-031 Lublin, Poland

rutile which contributes to the fact that it adsorbs mainly UV light (Daghrir et al. 2013; Zhang et al. 2014; Di Valentin et al. 2004).

According to the principles of green chemistry, materials, and also light sources available in the world should be used as effectively as possible (Anastas and Kirchhoff 2002). The Sun is such an inexhaustible light source. The light emitted by the Sun contains mainly radiation in the infrared ($\sim 52\%$) and visible ranges (Vis $\sim 43\%$) and only $\sim 5\%$ is UV radiation (Kumar and Devi 2011). Therefore for the effective exploitation of solar energy, it is necessary to obtain a photocatalyst with high activity at the visible light (Vis).

Obtaining a photocatalyst based on titanium oxide with high photocatalytic activity in the visible light (or solar light) area is a great challenge for the scientists. These properties can be obtained due to doping TiO_2 with: the nonmetals (Ho et al. 2006; Grabowska et al. 2009; Liu et al. 2006), the lanthanide ions (Silva et al. 2009; Aman et al. 2012; Yao et al. 2011; Wu et al. 2009) and the other transition metal elements (Kim et al. 2008; Inturi et al. 2014) or metal oxides (Bhachu et al. 2014; Banisharif et al. 2015). In addition, TiO_2 can be combined with the semiconductor having lower bandgap energy e.g. CdS (Hirai et al. 2001). Extremely favourable is obtaining TiO_2-based materials with the magnetic properties (Shojaei et al. 2015) or incorporating of the TiO_2 nanoparticles into the inert matrix (Thakur et al. 2015; Cho and Choi 2001; Chibac et al. 2017).

Such photocatalysts are produced in large amounts worldwide. However, their production methods are not often safe for the environment and create large amounts of waste products (Molchanov and Buyanov 2001). For the production of TiO_2-based photocatalysts, there can be used exemplary: the sol–gel method (Jraba et al. 2019; Arellano et al. 2018), applying Aloe Vera gel as fuel via solution combustion method (Kumar et al. 2020), temperature-regulated chemical vapor deposition (TR-CVD) (Saqlain et al. 2020), incorporating of TiO_2 into polymeric nanoparticles and their combinations with SiO_2/Fe_2O_3 (Chibac et al. 2017), photodeposition method from iron(III) nitrate precursors (Moniz et al. 2014), flame spray pyrolysis (Kokorin et al. 2017) and many others.

One of the methods not resulting in by-products is mechanical processes including the mechanochemical synthesis. It enables the preparation of different materials directly from initial materials e.g. loose powders (Kucio et al. 2019; Subramonian et al. 2017). Mechanochemical processes are most often carried out in various types of ball mills. High-energy planetary mills appear to be the most effective. The mechanical processes have many advantages: relatively low installation cost, the possibility of continuous and periodic work, as well as the ability to treat materials of different hardness (Miao et al. 2018). During collisions of grinding balls in the vessel, there is generated energy whose

value is so high that it allows direct synthesis of materials, e.g. photocatalysts (Kong et al. 2002). The effectiveness of mechanochemical processes depends, among others, on: mill rotation speed, time, temperature and atmosphere of milling (Baláž 2008; Suryanarayana 2001).

The aim of this paper was to use the environmentally friendly mechanochemical procedure to prepare nanocomposites with photocatalytic properties, also in the Vis range. The obtained photocatalysts contained TiO_2 (photocatalytic component), SiO_2 (adsorbent), and Fe_2O_3 as a source of iron ions (dopant). Photocatalytic activity of these materials was tested in relation to Methylene Blue (MB) in the range of ultraviolet radiation (UV) and visible light (Vis).

Experimental

Materials used

The materials used in the study were: TiO_2 (P-25, Sigma-Aldrich, Poland), SiO_2 (Si-60, Merck, Poland) and red Fe_2O_3 (POCh, Poland) as a Fe^{3+} source.

Preparation of photocatalysts

Photocatalysts were obtained as a result of mechanochemical synthesis (MChS) of initial materials in a planetary ball mill (Pulversitte 7 Premium Line, Fritsch, Germany). Powder milling was performed in two vessels. One of them was made of ZrO_2 (V = 80 cm³) and in this case, 250 small milling balls (ø = 3 mm) with ZrO_2 were used. The other vessel was made of Si_3N_4 and contained 25 Si_3N_4 balls of a larger diameter (ø = 10 mm). The mechanochemical synthesis was conducted at 250 or 500 rpm in the redistilled water presence at different milling times (1.5, 2, 4 h). After milling the composites were dried at 100 °C for 12 h. 7 samples with different initial materials were prepared (Table 1). The first sample contained

Table 1 Composition of individual samples and mechanochemical synthesis conditions

Sample	Composition	Milling time [h]*	Mill rotation speed [rpm]	Type of grinding vessel and balls
S-T	SiO_2, TiO_2	1.5	500	Si_3N_4
S-T$_C$	SiO_2, TiO_2	1.5	500	Si_3N_4
T-Fe$_{250}$	TiO_2, Fe_2O_3	4	250	ZrO_2
T-Fe$_{500}$	TiO_2, Fe_2O_3	2	500	ZrO_2
T-Fe$_{250H}$	TiO_2, Fe_2O_3	4	250	ZrO_2
T-Fe$_{250}$S-T	T-Fe$_{250}$, S-T	2	250	ZrO_2
T-Fe$_{250}$S-T$_C$	T-Fe$_{250}$, S-T$_C$	2	250	ZrO_2

*Milling was conducted in 15-min cycles with 5-min breaks between the cycles

only SiO_2 and TiO_2 was milled at 500 rpm. This sample was designated *S-T*. To check the effect of calcination on the photocatalytic activity (*S-T*), it was subjected to an additional heating process at 500 °C for 2 h (sample *S-T$_C$*). The TiO_2 content in the *S-T* and *S-T$_C$* composites was 28.6%w/w. The second series of composites contained TiO_2 and Fe_2O_3. The initial substrates were milled at 250 or 500 rpm and the obtained samples were designated *T-Fe$_{250}$* and *T-Fe$_{500}$* (the Fe_2O_3 content was 6.55%w/w of the total composite weight). The effect of higher temperature on the properties of *T-Fe$_{250}$* was examined by heating the sample at 200 °C for 2 h (sample *T-Fe$_{250H}$*).

After the preliminary studies of photocatalytic activity, it was found that the sample *T-Fe$_{500}$* had a lower photocatalytic activity compared to that of *T-Fe$_{250}$*. Thus, the *T-Fe$_{250}$* sample was used as a component to obtain 3-phase composites including equal proportions (w/w) of *S-T* (or *S-T$_C$*) and *T-Fe$_{250}$*. The obtained materials were designated: *T-Fe$_{250}$S-T* and *T-Fe$_{250}$S-T$_C$*. They contained 61%w/w of TiO_2, 35.7%w/w of SiO_2, and 3.3%w/w of Fe_2O_3.

Nitrogen adsorption/desorption

The nitrogen adsorption/desorption method at a low temperature (77.4 K) was used to determine the structural parameters of the obtained materials. Adsorption isotherms were recorded using a Micromeritics ASAP 2405 N (USA) adsorption analyzer. From the obtained data there were determined the characteristic structural parameters: the specific surface area (S_{BET} at p/p_0 between 0.06 and 0.2) and the pore volume (V_p, $p/p_0 \approx 0.98$) (Gregg and Sing 1982). To determine the pore size distributions ($f_V(R) \sim dV_p/dR$, PSD), the data from the desorption isotherm branch were used. The self-consistent regularization procedure (SCR) under the conditions of non-negative function of pore size distribution ($f(R_p) > 0$, $\alpha = 0.01$ as a fixed regularization parameter) was used (Gun'ko 2014). A model for the complex of pore types including slit-like pores shape (S), cylindrical pores shape (C), and voids between the pores (V) was applied. Using the procedure described by Gun'ko and Mikhalovsky (2004), the differential function was converted into an incremental pore size distribution ($dV/dR = f(R)$, IPSD$_V$). The differential functions were used to calculate: volume and surface area for the mesopores (V_{meso}, S_{meso}) and the micropores (V_{micro}, S_{micro}) as well as the deviation of the pore shape (Δw) (Table 2) (Charmas et al. 2017; Gun'ko and Do 2001).

Determination of macropores volume

The total pore volume (V_{total}) and macropore volume (V_{macro}) were determined by filling the pores of the samples with methanol. Initially, all samples were dried at 110 °C for 24 h. This was to eliminate physically adsorbed water. Then

Table 2 Parameters of the porous structure of the obtained nanophotocatalysts

Sample	S_{BET} [m² g⁻¹]	S_{micro} [m² g⁻¹]	S_{meso} [m² g⁻¹]	V_p [cm³ g⁻¹]	V_{micro} [cm³ g⁻¹]	V_{meso} [cm³ g⁻¹]	V_{total} [cm³ g⁻¹]	V_{macro} [cm³ g⁻¹]	R_{av} [nm]	R_{dom} [nm]	Δw
SiO$_2$ini	369.9	0.1	341.9	0.750	0.009	0.748	–	–	4.7	–	0.502
TiO$_2$ini	51.9	11.1	48.9	0.177	0.001	0.069	–	–	3.3	–	–0.908
Fe$_2$O$_3$ini	6.3	1.5	5.9	0.025	0.0001	0.011	–	–	4.2	–	0.416
S-T	299.5	29.0	275.9	0.590	0.008	0.536	1.15	0.560	5.8	0.9; 3.1; 9.0	0.253
S-T$_C$	293.5	20.4	276.0	0.597	0.005	0.545	1.17	0.573	6.1	0.9; 3.1; 9.0	0.260
T-Fe$_{250}$	50.4	0.3	48.8	0.292	0.0002	0.260	0.68	0.388	2.3	18.2	0.211
T-Fe$_{250H}$	46.6	1.5	44.6	0.281	0.0005	0.218	0.50	0.219	5.9	1.5; 17.9	0.884
T-Fe$_{500}$	51.8	1.9	49.6	0.227	0.0005	0.214	0.68	0.453	1.7	1.7; 14.3	0.199
T-Fe$_{250}$S-T	180.3	45.8	152.7	0.505	0.011	0.383	1.02	0.515	1.4	0.96; 3.0; 17.9	–0.665
T-Fe$_{250}$S-T$_C$	173.1	44.2	145.6	0.473	0.011	0.367	1.20	0.727	1.4	0.96; 3.0; 17.9	–0.685

S_{BET} the specific surface area, S_{micro} the surface area of micropores, S_{meso} the surface area of mesopores, V_p the sorption pores volume (from N_2 desorption data), V_{micro} the volume of micropores, V_{meso} the volume of mesopores, V_{total} the pores volume determined using methanol, V_{macro} the macropores volume determined using methanol, R_{av} the average pore radius, R_{dom} the dominating pore radius, Δw the roughness

the 0.2 g samples were weighed and placed in small flasks ($V = 25$ cm^3). Methanol was added to the sample dropwise using a glass analytical burette ($V = 1$ cm^3). Next the flasks were placed in an ultrasonic bath which allowed better penetration of the pores by alcohol.

The titration procedure was repeated three times. After filling the pores, the volume of added methanol ($V_{methanol}$) was used to determine the total pore volume (V_{total}) according to Eq. 1:

$$V_{total} = V_{met} / m_s \tag{1}$$

where: V_{total}—the pores volume determined using methanol [cm^3 g^{-1}]; V_{met}—the average volume of the methanol filling pores [cm^3]; m$_s$ – the sample mass [g].

Next using V_{total}, the macropores volume (V_{macro}) was calculated from Eq. 2:

$$V_{macro} = V_{total} - V_p \tag{2}$$

where: V_{macro} – the volume of macropores [cm^3 g^{-1}]; V_{total}— the total pores volume [cm^3 g^{-1}]; V$_p$ – the sorption pores volume, the data obtained on the basis of N$_2$ adsorption/desorption [cm^3 g^{-1}].

XRD analysis

Structural analysis of the materials was performed using X-ray powder diffractometer (PANalytical, Empyrean, Netherlands) at the tension of 40 kV and the current of 10 mA. The monochromatic Al Kα radiation was used. The crystallite sizes were calculated using the Scherrer equation.

Spectroscopic characteristics

The Fourier transformed photoacoustic infrared spectra (FT-IR/PAS) of the examined samples were recorded by means of the Bio-Rad Excalibur FT-IR 3000 MX spectrometer over the 4000—400 cm^{-1} range at room temperature, the resolution 4 cm^{-1}, the mirror velocity 2.5 kHz and the maximum source aperture, using the MTEC Model 300 photoacoustic cell. Dry helium was used to purge the photoacoustic cell before data collection. The spectra were normalized by computing the ratio of a sample spectrum to that of the MTEC carbon black standard. A stainless steel cup (ø = 10 mm) was filled with the sample (thickness < 6 mm) and interferograms of 1024 scans were averaged for the spectrum, providing a good signal-to-noise (S/N) ratio. No smoothing functions were used. All spectral measurements were performed at least in triplicate.

Thermal analysis

To determine the thermal properties of the samples, thermal analysis was performed using a Derivatograph C (Paulik, Paulik & Erdey, MOM, Budapest). The tested material was placed in a small corundum crucible. The sample weights were about 30 mg. Al$_2$O$_3$ was used as the reference sample. The analysis was made in the air atmosphere in the temperature range from 20 to 1000 °C (heating rate 10 °C min^{-1}). The TG, DTG, and DTA curves were registered.

Photocatalytic activity studies

Photocatalytic activity of the obtained samples was studied using the standard dye, Methylene Blue (MB, C$_{16}$H$_{18}$ClN$_3$S, initial concentration C$_0 = 1 * 10^{-5}$ mol L^{-1}) at the ultraviolet radiation (UV) and visible light (Vis). The ratio of solution (MB) to the sample weight was 1:1. The MB solution with the tested photocatalyst was placed on the magnetic stirrer to provide a homogeneous reaction environment. Before turning on the light source, a 30-min step of surface dye adsorption in the dark took place. When the light was on, the samples of solution were taken at regular intervals and filtered using syringe filters and centrifuged to get rid of the photocatalyst. The solution concentrations were measured using the UV – Vis spectrophotometer (Helios Gamma, Spectro-Lab, Poland) based on the calibration curve $y = 0.061x$ ($R^2 = 0.9986$). The efficiency of the MB degradation (η) was calculated using the following Eq. 3 (Rožić et. al 2019):

$$\eta = \frac{C_0 - C}{C_0} \cdot 100 \tag{3}$$

where: η – the efficiency of the MB degradation [%]; C_0 – the initial concentration of MB [mol L^{-1}]; C – the concentration [mol L^{-1}] of MB after t minutes of irradiation.

Ultraviolet radiation (UV)

The photocatalytic test was carried out in a glass three-necked reactor (UV-RS-2, Heraeus). The UV radiation source was a quartz lamp (150 W cm^{-2}) placed in the solution. The experiment was conducted for 45 min.

Visible light (Vis)

In the case of exposure to visible light, the experiment was conducted for 22 h. The solution of MB with the tested sample was placed in a glass beaker ($V = 500$ mL). The source of

visible light was an LED electric bulb (50 mW cm^{-2}) which was located 20 cm above the solution. All experiments were conducted at room temperature.

Results and discussion

Figure 1 shows the low-temperature nitrogen adsorption/desorption isotherms (Fig. 1a) and pore sizes distribution curves (Fig. 1b,c) for the obtained materials. In all cases, according to the IUPAC classification (Rouquerol et al. 1994), they are type IV isotherms, which are characteristic of mesoporous materials, in the pores of which the phenomenon of capillary condensation is observed. In the case of

S-T and S-T_C materials, the course of isotherms curves is almost identical which suggests that calcination at 500 °C did not cause significant changes in the porous structure of the material. A thorough analysis of the hysteresis loop shape indicates that they are not symmetrical. This may indicate a bimodal nature of these materials. They contain a small amount of micropores. This is evidenced by the rather intense increase of adsorption in the area where the relative pressure is very low ($p/p_0 < 0.1$). The shape of the hysteresis loops at $p/p_0 = 0.5$—0.8 indicates the presence of mesopores while the increase of adsorption in the range of relative pressure $p/p_0 = 0.9$–1 indicates the presence of wide pores. This is also confirmed by the functions of their pore volume distribution as shown by two maxima (Fig. 1b).
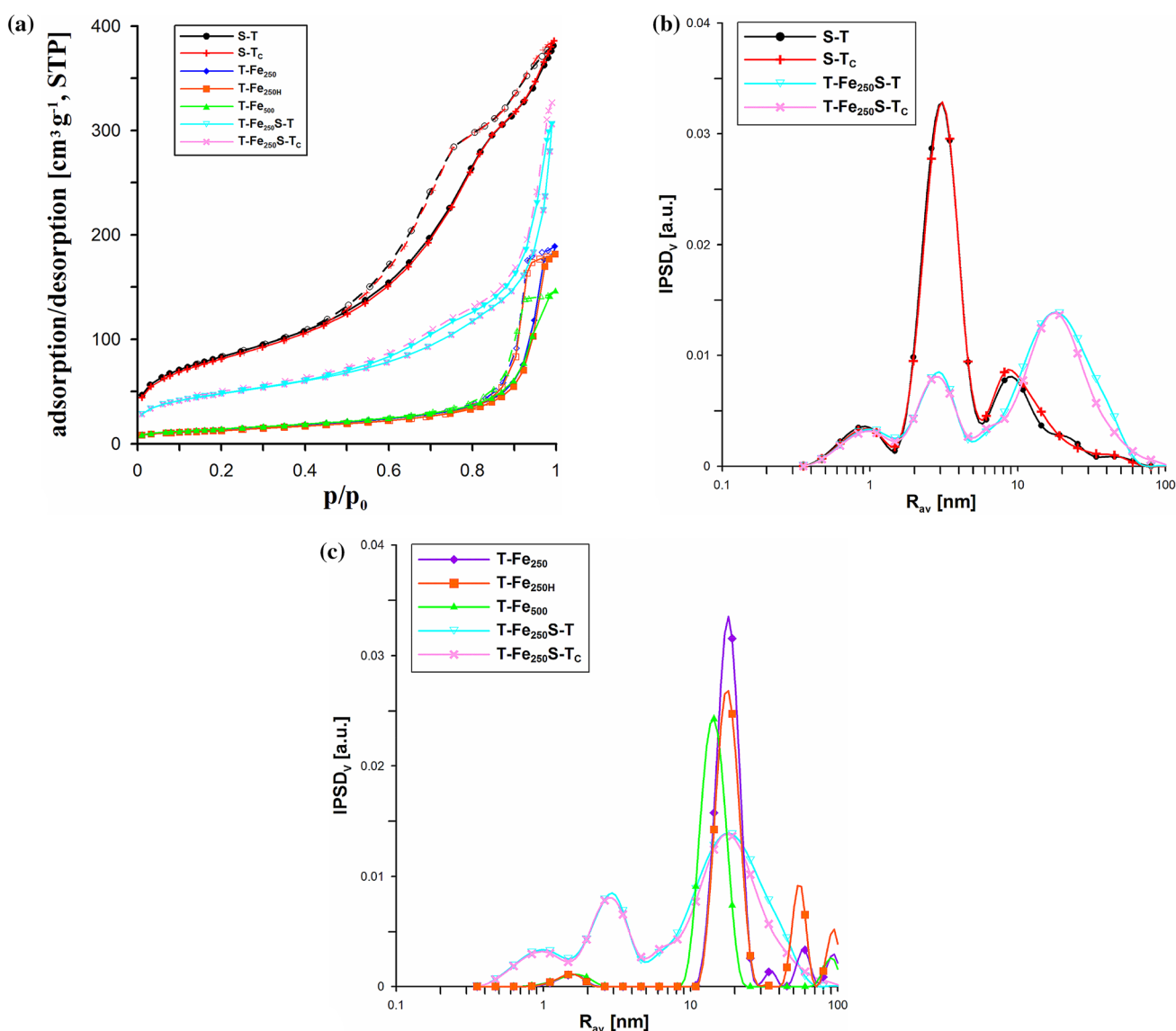

Fig. 1 Low-temperature nitrogen adsorption/desorption isotherms (**a**) and incremental pore size distribution curves (IPSDV; **b**,**c**) for the tested materials

Analyzing the shape of the isotherms obtained for the $T\text{-}Fe_{250}$, $T\text{-}Fe_{500}$, and $T\text{-}Fe_{250H}$ composites (Fig. 1a), one can observe that isotherms in the area of relative pressure $p/p_0 < 0.1$ are located very low. This suggests a minimum number of micropores. In the range $p/p_0 = 0.1$–0.7, the isotherms have a course almost parallel to the axis of relative pressure which is the evidence of the lack of narrow mesopores (Fig. 1a). For these materials hysteresis loops appear in the area of relative pressures above $p/p_0 > 0.9$. In this range the course of isotherms is steep, indicating the presence of wide pores. The hysteresis loops are relatively symmetrical which evidences the existence of homogeneous size pores in these materials (Fig. 1a). The shape of the isotherms obtained for the $T\text{-}Fe_{250}S\text{-}T$ and $T\text{-}Fe_{250}S\text{-}T_C$ composites can be taken as intermediate in relation to the previously discussed types of isotherms (Fig. 1a). This points out that the structure of the materials is similar to that of constituent components. In this case the additional calcination did not change the structure either. The course of adsorption isotherms suggests a smaller number of micropores and mesopores compared to $S\text{-}T$ and $S\text{-}T_C$ (Fig. 1a). Figure 1 b,c presents the incremental pore size distribution ($IPSD_V$) curves relative to their average radii for the tested materials. The curves obtained for the $S\text{-}T$ and $S\text{-}T_C$ materials have a very similar course which confirms that the additional calcination step did not change their porous structure (Fig. 1b). These composites have pores with a dominant radius $R_{dom} \sim 3$ nm and a small number of pores with a radius ~ 9 nm (Fig. 1b). The porous structure of these materials is closely related to the characteristics of the initial materials (Table 2). It is known that during the mechanochemical treatment the surface and porosity of materials diminish. Also in the case of $T\text{-}Fe_{250}$ and $T\text{-}Fe_{250H}$ materials, the curves are almost identical (Fig. 1c). Clearly defined maxima occur at $R_{dom} \sim 18$ nm (Fig. 1c). It follows that the additional heating of the composite at 200 °C had no effect. Comparing the materials $T\text{-}Fe_{250}$ and $T\text{-}Fe_{500}$ it can be concluded that increasing of mill rotation speed while reducing milling time resulted in the dominant pore radius being reduced ($R_{dom} \sim 14$ nm). The other small maximum is at about 1.5 nm. The dV/dR curves of the $T\text{-}Fe_{250}S\text{-}T$ and $T\text{-}Fe_{250}S\text{-}T_C$ composites confirm the biporosity of these materials. There are pores with the dominant radii $R_{dom} \sim 3$ nm and ~ 18 nm (Fig. 1b,c). The course of these curves may suggest that the extension of the modification time (after milling $S\text{-}T$ and $S\text{-}T_C$ were again milled with the addition of $T\text{-}Fe_{250}$ at a speed of 250 rpm) and increasing the mill rotation speed have a positive effect on the creation of micropores (Fig. 1c; Table 2).

Table 2 presents the porous structure parameters determined for the obtained materials. The analysis of these data indicates that the materials have a differentiated specific surface area. The materials with a large SiO_2 content have a developed specific surface area S_{BET} of about 300 m^2 g^{-1} ($S\text{-}T$, $S\text{-}T_C$). For the materials prepared based on TiO_2 ($T\text{-}Fe_{250}$, $T\text{-}Fe_{250H}$, $T\text{-}Fe_{500}$) the specific surface areas are about 50 m^2 g^{-1}. It was observed that the additional calcination caused a slight reduction of this parameter ($T\text{-}Fe_{250H}$, $S_{BET} = 46.6$ m^2 g^{-1}) while the increase of rotation speed did not significantly affect the specific surface area ($T\text{-}Fe_{500}$, $S_{BET} = 51.8$ m^2 g^{-1}). The sorption pore volume (V_p) is the largest for the $S\text{-}T_C$ material ($V_p = 0.597$ cm^3 g^{-1}). The lowest value of $V_p = 0.227$ cm^3 g^{-1} is found for the $T\text{-}Fe_{500}$ material, which was milled at 500 rpm. For $T\text{-}Fe_{250}$, which was milled at 250 rpm, this value is slightly higher ($V_p = 0.292$ cm^3 g^{-1}) (Table 2). The highest value of $V_{total} = 1.17$ cm^3 g^{-1} is found for the $S\text{-}T_C$ sample and the highest $V_{macro} = 0.727$ cm^3 g^{-1} for the $T\text{-}Fe_{250}S\text{-}T_C$ sample. In this case the significant increase in the pore volume is mainly due to the intense modification of the SiO_2 structure under high-temperature conditions (Leboda and Mendyk 1982). The deviations from the assumed pore shape were also calculated (Δw) and they were from -0.908 (TiO_2ini) to 0.884 ($T\text{-}Fe_{250H}$, Table 2). The values of S_{micro} and V_{micro} are small because these materials are mesoporous (Table 2). Similar values of the structural parameters for the materials of $Fe_2O_3\text{-}TiO_2$ type were found by Subramonian (Subramonian et al. 2017).

The XRD spectra of the tested photocatalysts show that anatase and rutile are present in the samples (Fig. 2). The calculated crystallite sizes are given in Table 3. The XRD pattern shows peaks at $2\theta = 25.3°$ (101), $37.9°$ (004), $48.1°$ (200), $54.1°$ (105), $55.1°$ (211), $62.9°$ (204) and $75.0°$ (215) planes (JCPDS Card No. 04–014-5762). There are also peaks at $2\theta = 27.4°$ (110), $36.1°$ (101) and $41.3°$ characteristic of the rutile phase (JCPDS Card No. 01–076-1938) as well as peaks at $2\theta = 24°$ (012), $33.1°$ (104), $35.6°$ (110), $41.2°$ (113), $49.5°$ (024) and $64.1°$ (300) planes which correspond to Fe_2O_3 (JCPDS Card No. 04-015-9571). The peaks characteristic of rutile-TiO_2 and Fe_2O_3 are very low due to the small proportion of these phases in the composite structure. For the materials with a lower Fe_2O_3 content (1%Fe), peaks from this phase are not detected (Saqlain et al. 2020). These results are consistent with the literature data (Ganesh et al. 2012; Kumar et al. 2020; Chibac et al. 2017; Kokorin et al. 2017).

TiO_2ini is composed of the mixed phases that is 89% anatase and 11% rutile. The additional heating of the $T\text{-}Fe_{250}$ at 200 °C for 2 h ($T\text{-}Fe_{250H}$) increased the anatase phase content by about 1.5% compared to the $T\text{-}Fe_{250}$ material. In the case of $S\text{-}T$ sample, the additional calcination at 500 °C reduced the proportion of anatase phase-only insignificantly ($S\text{-}T_C$). $T\text{-}Fe_{250}$ has the largest size of anatase crystals (26.0 nm) and contains the most anatase phase (81.8%) of all the samples. In the case of $T\text{-}Fe_{500}$, which contains the most rutile phase (12.7%), the sizes of rutile crystals are the largest (39.3 nm, Table 3). The lack of characteristic
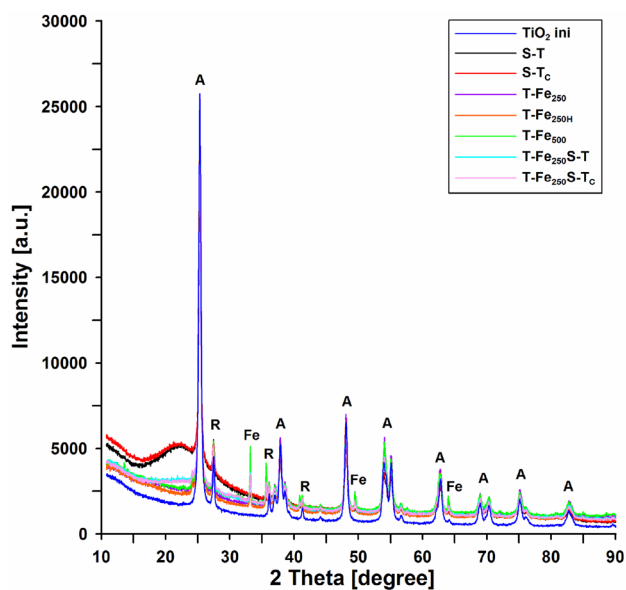
Fig. 2 XRD spectra of the obtained photocatalysts

Table 3 Physical properties of tested materials obtained from the XRD analysis

Sample	TiO_2 crystalline form	Crystallite size [nm]	TiO_2 crystalline phases content [%]
$TiO_{2\,ini}$	A	23.2	89.0
	R	36.8	11.0
S-T	A	22.8	91.0
	R	37.7	9.0
S-T_C	A	23.1	90
	R	35.6	10
T-Fe_{250}	A	26.0	81.8
	R	27.9	11.1
T-Fe_{250H}	A	23.9	83.4
	R	38.0	10.8
T-Fe_{500}	A	23.6	79.3
	R	39.3	12.7
T-$Fe_{250}S$-T	A	23.7	84.7
	R	37.3	10.5
T-$Fe_{250}S$-T_C	A	23.8	84.3
	R	37.1	10.8

A anatase, *R* rutile

SiO_2 bands is due to the fact that this component has an amorphous form.

The FT-IR/PAS spectra of the studied samples are presented in Fig. 3 a, b. The main bands at 4000–2400 cm^{-1} are the vibrations of hydroxyl groups (3745 cm^{-1} – the isolated silanol groups ≡SiOH, 3691 cm^{-1} – the isolated –OH in TiO_2 and/or Fe_2O_3, and 3677 cm^{-1} – the hydrogen-bonded –OH···H) (Fig. 3a). Among the spectra of the samples containing SiO_2 the band intensity of isolated –OH groups is the highest for the S-T_C sample and decreases for the T-Fe_{250}S-T and T-Fe_{250}S-T_C spectra. Those bands do not occur for the samples without silica, however, the bands of isolated hydroxyl groups in the samples containing TiO_2 and Fe_2O_3 shift towards lower wavenumbers (3691 cm^{-1}). Their intensity is the highest in the case of the T-Fe_{250} sample spectrum. The peaks with the maximum at ~3660 cm^{-1} are responsible for the presence of hydrogen-bonded SiOH···–OSi groups presence, and more precisely this indicates the occurrence of internal hydroxyl groups. The wideband with the maximum at ~3430 cm^{-1} shows both –OH and hydrogen-bonded –OH···H in the oxide structures and physically adsorbed water (Fig. 3a).

In the spectra of the samples containing silica, the broad, intense bands in the range of 1300–1000 cm^{-1} can be attributed to the asymmetric stretching vibrations of Si–O–Si bridges and the peaks at ~795 cm^{-1} and ~470 cm^{-1} can be assigned to the symmetric stretching and deformation modes of Si–O–Si, respectively (Fig. 3b). The IR bands observed within 980–910 cm^{-1} can be assigned to the Si–O–Si stretching vibrations. The bands at 970 cm^{-1} are visible in the spectra of all samples containing silica, however, their intensity differs for the spectra of the samples containing TiO_2 and Fe_2O_3 – a new band appears at ~941 cm^{-1}. Additionally, the lower intensity of 940 cm^{-1} band compared to the band at ~795 cm^{-1} (symmetric Si–O-Si vibrations) may be the evidence of titania ions attachment to the crystal lattice of silica. The band at ~795 cm^{-1} is invisible in the T-Fe_{250}S-T and T-Fe_{250}S-T_C spectra. No structural changes are visible for the samples without silica (T-Fe_{250H}, T-Fe_{250}, T-Fe_{500}) (Fig. 3b).

Thermal analysis was used to estimate the thermal stability of the materials. Figure 4 shows the course of the TG (a, c) and DTG (b, d) curves registered for the tested materials. In the case of SiO_2 containing materials, the recorded weight loss occurs in two stages, the first in the range of 0–200 °C and the second one at 200–1000 °C. In all materials the first stage occurs very intensively, which is associated with the desorption of physically bound water (20–200 °C). The weight loss to a temperature 200 °C for the *S-T* material is ~2.7% and for *S-T_C* ~2.4% (Fig. 4a). These values are typical of the SiO_2/TiO_2 composite materials (Skubiszewska et al. 2012). For the *S-T* and *S-T_C* materials the second stage is slower and it is associated with dehydroxylation of SiO_2 surface groups (Charmas et al. 2019). The total weight loss for the S-*T* material is ~4.6% and for *S-T_C* ~5.1% (Fig. 4a). For the *T-Fe_{250}S-T* and *T-Fe_{250}S-T_C* materials the course of TG curves (Fig. 4a) is different and the total weight loss is greater (~6.5%). At a temperature higher than 800 °C the weight did not change. The dominant component in these materials is

Fig. 3 FT-IR/PAS spectra of the studied samples in **a** 4000–2400 cm-1 range, **b** 2000–400 cm-1 range
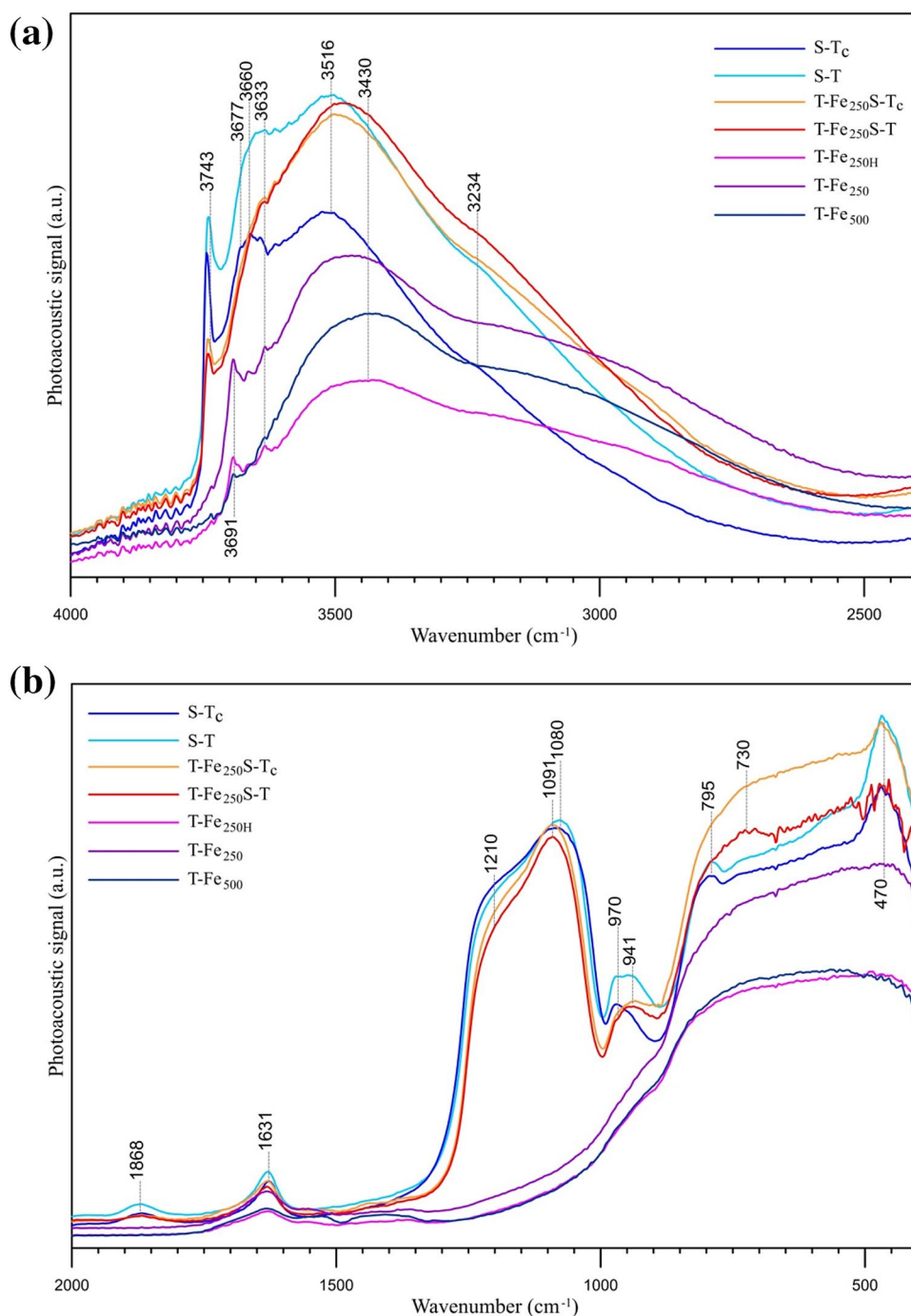
TiO$_2$ (61%). The significant difference observed for individual materials is due to the different polarities of their surface. The DTG (Fig. 4b) and DTA (not shown here) curves also confirm the changes. For the *S-T* sample the maximum weight loss rate is ~0.065 mg min^{-1} and for *S-T$_C$* ~0.068 mg min^{-1} (Fig. 4b). For the samples containing TiO$_2$ and Fe$_2$O$_3$ the weight loss caused by the water loss is not so intensive (Fig. 4c). This is due to the structure and low specific surface area (S$_{BET}$) of the components (Tab. 2). Above 400 °C the weight stabilization

of *T-Fe$_{500}$* (~2.6%) and *T-Fe$_{250H}$* (~3.1%) materials is observed. However, for the *T-Fe$_{250}$* photocatalyst the reduction of mass is observed to ~800 °C, and the maximum weight loss is 4.2% (Fig. 4c). Further heating of these materials does not cause significant weight changes (Fig. 4c). The additional heating after preparation of *T-Fe$_{250H}$* and the mechanochemical synthesis carried out at a higher mill rotation speed (500 rpm, *T-Fe$_{500}$*) resulted in a decrease in the water amount in these materials compared to the *T-Fe$_{250}$* sample. This is also proved by the
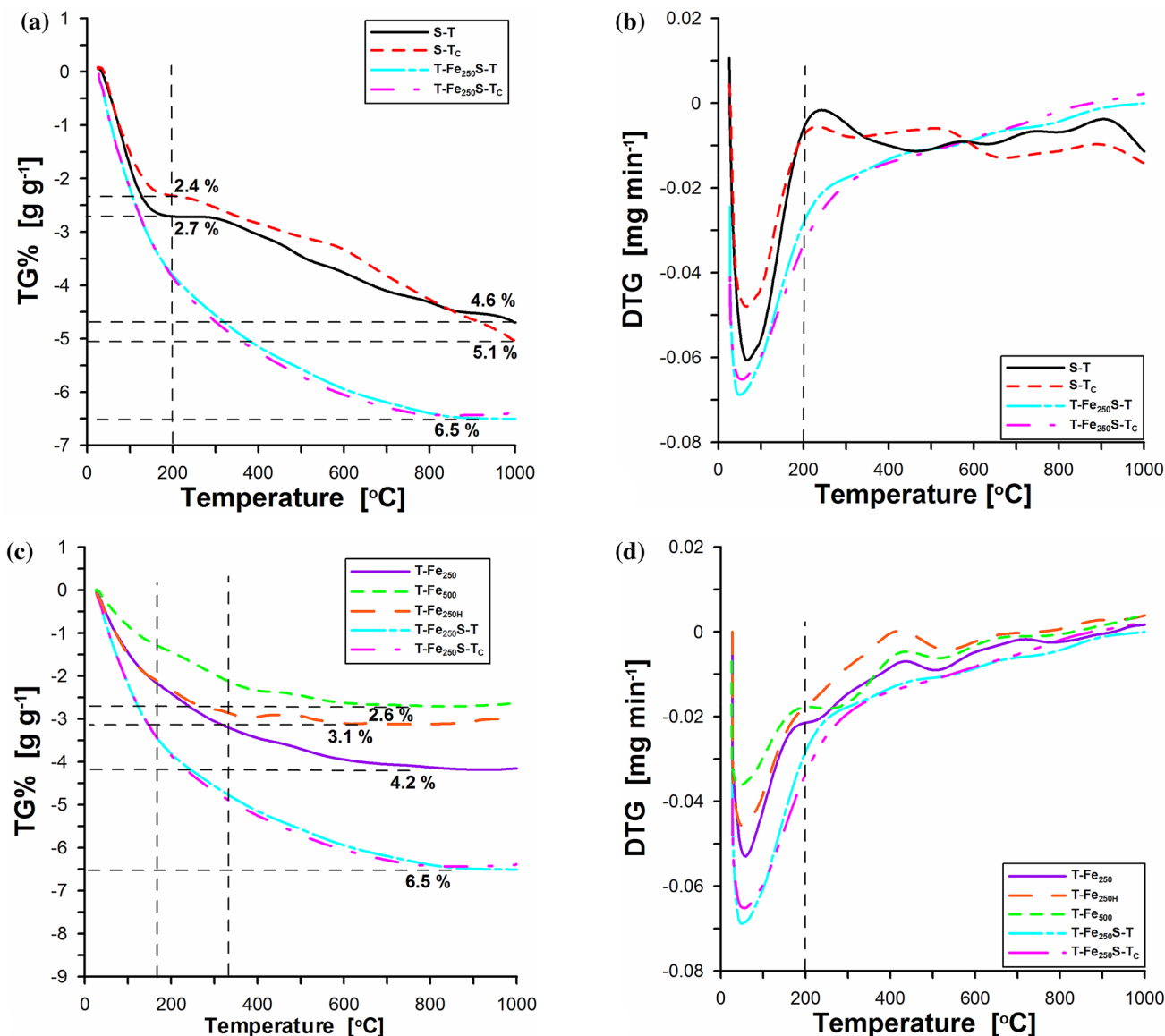
Fig. 4 The course of TG (**a,c**) and DTG (**b,d**) curves for the tested materials

DTG curves which show that the mass-loss rates for the $T\text{-}Fe_{250}$, $T\text{-}Fe_{250H}$ and $T\text{-}Fe_{500}$ materials were 0.05; 0.045 and 0.035 mg min^{-1}, respectively (Fig. 4d).

Photocatalytic tests were carried out for all obtained materials. After 30 min in the dark, different amounts of dye adsorption were observed on the photocatalysts surface. From the course of the analyzed curves it results that the highest amount of adsorption was using the materials containing large amounts of SiO_2: $S\text{-}T$ and $S\text{-}T_C$ (Fig. 5). This is due to the significant participation of the SiO_2 surface in the composite and the dye adsorption on its porous, hydrophilic surface of this component (Table 2). Calcination changed slightly the structure and porosity of the $S\text{-}T$ surface (Table 2) but increased the efficiency of adsorption ($S\text{-}T_C$).

This may be due to the increase in pore size as a result of calcination which has become more accessible for the adsorbed dye molecules. Silica is a very effective adsorbent, the MB concentration after adsorption is reduced by ~ 75% and ~ 90% for the $S\text{-}T$ and $S\text{-}T_C$ materials, respectively.

The lower adsorption (~ 60%) was observed on the $T\text{-}Fe_{250}S\text{-}T$ and $T\text{-}Fe_{250}S\text{-}T_C$ composites. This is due to the change in the ratio of individual components content in the composites. The smallest adsorption ability was exhibited by the $T\text{-}Fe_{250}$, $T\text{-}Fe_{250H}$ and $T\text{-}Fe_{500}$ materials (about 40%, Fig. 5), due to their small surface area of these materials compared to those containing the SiO_2 phase. Thus, adsorption on the $S\text{-}T_C$ is almost 3 times more effective than on the $T\text{-}Fe_{250}$ sample because of the significant difference in the
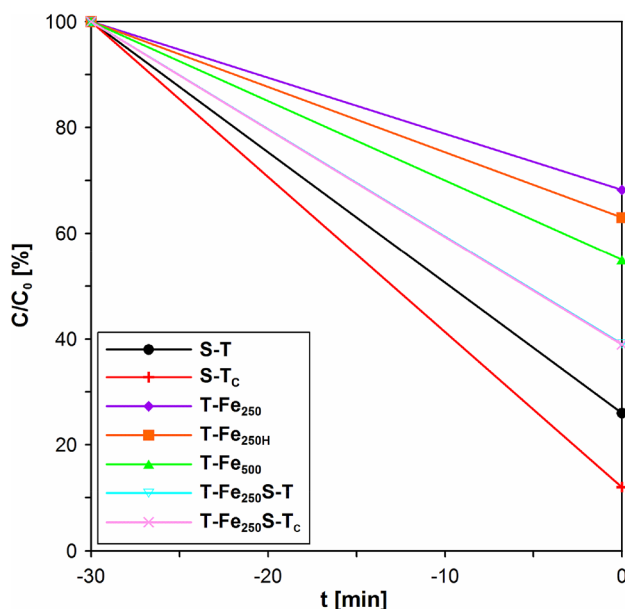
Fig. 5 Changes in the dye concentration (MB) after a 30-min adsorption process on the tested photocatalysts in the dark

specific surface area of silica and titanium oxide photocatalysts. The specific surface area of silica is 7 times larger than that of TiO₂ (Table 2).

Figure 6 a and b presents the changes in the concentration of MB solution irradiated with UV and visible light (Vis) in the presence of the obtained photocatalysts. Changes in the dye concentration after the adsorption stage are significant (Fig. 5) therefore additionally, the effects of photocatalysts

are presented using the dye concentration after adsorption as the initial dye concentration (Fig. 6). This action allowed studying the actual photocatalytic activity of the obtained materials.

Ultraviolet radiation (UV)

The course of the curves in Fig. 6a shows that the use of the obtained photocatalysts accelerated significantly dye degradation which occurs at different speeds. The experiment was conducted for 45 min. The first stage of dye degradation is very intense and lasts 5 min. The most effective photocatalyst in this stage is the *T-Fe₂₅₀S-T* sample. In the second stage the reduction of MB concentration is systematic and slow. The most effective changes are observed using the *S-T* sample. In the presence of this material, dye degradation after 45 min of irradiation was 7 times more effective than decomposition of MB without a photocatalyst (Fig. 6a). For this material this may be associated with simultaneous photocatalysis and adsorption. Based on the course of the curves it can be also concluded that the calcination stage affects negatively the photocatalytic activity of the *S-T*$_C$ and *T-Fe₂₅₀S-T*$_C$ samples. For both materials photocatalysis has a similar course. The first stage is very intense (about 5 min) while the second one is much slower.

The results of MB degradation at UV radiation using the *S-T* and *S-T*$_C$ materials after 45 min show clearly that the *S-T* sample is more effective than the *S-T*$_C$ one. After 45 min of photocatalysis the efficiency is 100% for the *S-T* sample while after calcination (*S-T*$_C$ sample) this value is lower being 83% (Table 4). The effect of calcination is more
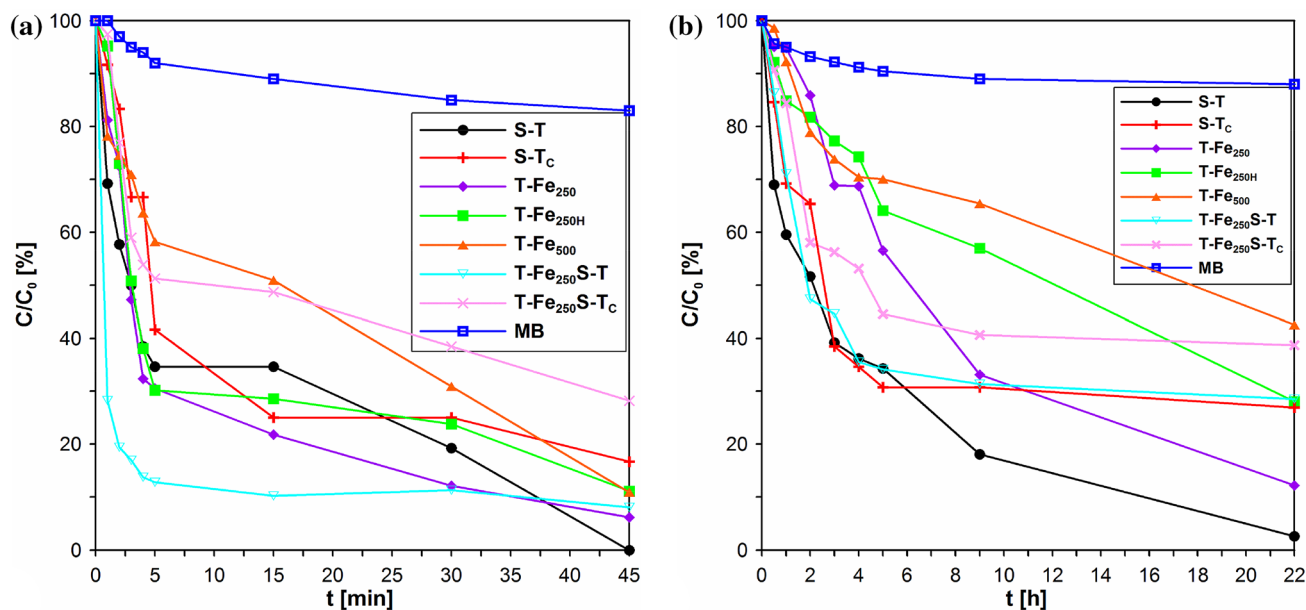

Fig. 6 Photocatalytic removal of MB by the usage of UV(**a**) and VIS (**b**) determined using UV–Vis spectroscopy

clearly visible for the *T-Fe$_{250}$S-T* and *T-Fe$_{250}$S-T$_C$* materials. After 5 min of UV irradiation of the MB solution in the presence of *T-Fe$_{250}$S-T$_C$* about 50% of the dye is degraded while the non-calcined material (*T-Fe$_{250}$S-T*) is almost twice more effective. After 45 min of exposure, the MB degradation rate for these materials is 72% for *T-Fe$_{250}$S-T$_C$* and 92% for *T-Fe$_{250}$S-T* (Table 4). In the case of *T-Fe$_{250}$*, *T-Fe$_{250H}$*, *T-Fe$_{500}$* both additional heating of the obtained photocatalyst and the increasing number of revolutions during the mechanochemical treatment do not have a positive effect on promoting the photocatalytic activity of materials (Fig. 6a).

Visible light (Vis)

Coupling of Fe$_2$O$_3$ with TiO$_2$ improves light absorption ability and optical properties because of the bandgap reduction (2.95 eV) of Fe$_2$O$_3$-TiO$_2$ as compared to P25 (3.35 eV, Subramonian et al. 2017). The lower bandgap of Fe$_2$O3-TiO$_2$ was due to electronic coupling between the wide bandgap of TiO$_2$ and the narrow bandgap of Fe$_2$O$_3$ (Wang et al. 2013). As a result, the new composite becomes active in the visible light area.

Figure 6b shows the dye photodegradation in the presence of the obtained materials using visible light. As the efficiency of photocatalysis using the TiO$_2$-based catalysts affected by visible light is relatively slow, the experiments were conducted for 22 h. The photodegradation of dye is different compared to that at UV irradiation (Fig. 6a). The initial stage of photodegradation was less effective and lasted

Table 4 Efficiency of the MB degradation η depending on the type of radiation

Type and time of radiation	Sample	Efficiency of degradation η [%]
UV[45 min]	*S-T*	100
	S-T$_C$	83
	T-Fe$_{250}$	94
	T-Fe$_{250H}$	89
	T-Fe$_{500}$	89
	T-Fe$_{250}$S-T	92
	T-Fe$_{250}$S-T$_C$	72
	MB*	17
Vis[22 h]	*S-T*	97
	S-T$_C$	73
	T-Fe$_{250}$	88
	T-Fe$_{250H}$	72
	T-Fe$_{500}$	57
	T-Fe$_{250}$S-T	71
	T-Fe$_{250}$S-T$_C$	61
	MB*	12

MB* *the* irradiated Methylene Blue solution without a photocatalyst

4–6 h. The degradation efficiency was from ∼20 to ∼70% depending on the material. Such values of degradation efficiency are close to those presented in (Jraba et al. 2019). In this stage, the most effective materials are *S-T* and *S-T$_C$*. In the second stage a further slowdown of the process takes place; however, after ∼22 h the process efficiency appears to be only slightly smaller to thar with the UV irradiation influence (Fig. 6a,b). Such observations are in line with literature reports (Jraba et al. 2019). In fact, the duration of the photocatalysis process in the UV and Vis areas differed significantly (45 min vs. 22 h) which is unfavourable from a technological point of view but the possibility of using sunlight makes such processes preferable.

In the case of the *T-Fe$_{250}$*, *T-Fe$_{250H}$*, *T-Fe$_{500}$* photocatalysts, which have the same composition, the highest photocatalytic activity was exhibited by the *T-Fe$_{250}$* sample. The degradation efficiency was ∼88% (Tab. 4). The mechanochemical synthesis using TiO$_2$ and Fe$_2$O$_3$ carried out at the increased mill speed (500 rpm) did not affect positively the activity of *T-Fe$_{500}$* material. Dye degradation with this photocatalyst was about 70%. The additional heating of the *T-Fe$_{250}$* sample (200 °C, *T-Fe$_{250H}$*) contributed to the reduction of MB degradation to about 57% (Fig. 6b, Table 4). For the material prepared based on the *S-T* material (*T-Fe$_{250}$S-T*), it was observed that after 22 h of irradiation with the visible light, 71% of the dye was degraded. The additional calcination of this material (*T-Fe$_{250}$S-T$_C$*) reduced activity and degradation efficiency to 61% (Table 4). The negative impact of calcination on the photocatalytic activity of materials has been confirmed, for example by Arellano et al. (Arellano et al. 2018), however, some research results indicate an inverse relationship (Saqlain et al. 2020).

Kinetics of photocatalytic degradation of MB

The rate constants k$_1$ were calculated from Eq. 4 (Buda and Czech 2013):

$$-ln\frac{C}{C_0} = k_1 \bullet t \qquad (4)$$

where: C_0 - the initial concentration of MB [mol L^{-1}], C— the concentration [mol L^{-1}] of MB after *t* minutes of irradiation, k_1—the pseudo-first order rate constant (min^{-1}) which were calculated on the basis of plotting: –ln(c/c$_0$) vs. time.

In addition, the apparent rate catalyst constant per the specific surface area (S$_{BET}$) unit (k$_S$) was estimated. For this purpose Eq. 5 was used (Buda and Czech 2013):

$$k_S = \frac{k_1}{m_p \bullet V_s \bullet S_{BET}} \qquad (5)$$

Table 5 The kinetic parameters of MB removal

Sample	UV				VIS			
	k_1 [min^{-1}]	k_S [min^{-1} m^2]	T ½ [min]	R^2	k_1 [h^{-1}]	k_S [h^{-1} m^{-2}]	T 1/2 [h]	R^2
S-T	0.206	0.06878	3.36	0.973	0.197	0.06578	3.52	0.8929
S-T$_C$	0.159	0.05417	4.36	0.884	0.244	0.08314	2.84	0.9538
T-Fe$_{250}$	0.261	0.51786	2.66	0.961	0.113	0.22421	6.13	0.959
T-Fe$_{250H}$	0.260	0.55794	2.67	0.971	0.076	0.16309	9.12	0.946
T-Fe$_{500}$	0.096	0.18533	7.22	0.928	0.081	0.15637	8.56	0.919
T-Fe$_{250}$S-T	0.359	0.19911	1.93	0.770	0.222	0.12313	3.12	0.930
T-Fe$_{250}$S-T$_C$	0.154	0.08886	4.50	0.941	0.160	0.092325	4.33	0.927

where: m_p – the mass of the photocatalyst [g], V_s – the volume of MB solution [L], S_{BET}—the specific surface area [m^2 g^{-1}] of the tested photocatalyst.

The half-lives ($t_{1/2}$) were also estimated based on Eq. 6 (Buda and Czech 2013):

$$t_{1/2} = \frac{ln2}{k_1} \qquad (6)$$

Based on the obtained data the removal process of MB can be described by the pseudo-first-order kinetics. In the case of UV irradiation the kinetic parameters were calculated for the first 5 min when the process was the fastest (Table 5). The highest k_1 value was observed at the UV exposure in the presence of the *T-Fe$_{250}$S-T* photocatalyst ($k_1 = 0.359$ min^{-1}). The dye removal was the slowest in the presence of the sample *T-Fe$_{500}$*, where k_1 value was 0.096 min^{-1}. In the case of Vis light the kinetic parameters were estimated for up to 5 h. At the time from 0 to 5 h the dye removal process was the fastest. For the *S-T$_C$* sample the k_1 value was 0.244 h^{-1} and in the presence of this sample the process of MB removal was the fastest. The slowest process was observed in the presence of *T-Fe$_{250H}$* $k_1 = 0.076$ h^{-1} (Table 5).

Conclusions

Structural, thermal, and photocatalytic properties of composite materials containing SiO_2, TiO_2, and Fe_2O_3 as a source of iron ions were studied. It was shown that mechanochemical synthesis in a high-energy planetary mill enables the effective preparation of composite materials with photocatalytic properties. The effect of greater mill rotation speed and the additional calcinations of materials was also investigated. The data obtained on the basis of low-temperature nitrogen adsorption/desorption indicate clearly that these materials are mesoporous. The tested photocatalysts contained both the anatase (in a greater quantity) and the rutile phases. The materials with the addition of SiO_2 are characterized by better MB adsorption compared to the others. This is due to the significant share of SiO_2 surfaces in the photocatalysts structure. The thermal analysis showed that the materials are characterized by significant thermal stability. The desorption of water physically bound to the surface of the materials proceeded up to 200 °C. The obtained materials are characterized by a photocatalytic activity in the presence of both UV irradiation and visible light (Vis). When UV was used as a source of light, the *S-T* sample was the most active. After 45 min of irradiation a complete dye degradation was observed while in the absence of photocatalysts only 17% of MB was degraded. This sample also exhibited the highest photoactivity in the presence of visible light (Vis). After 22 h 97% of the dye was degraded. Under these conditions MB without the addition of photocatalysts degraded in only 12%. Both the additional calcinations and the use of faster mill rotation speed did not improve the photocatalytic activity of the samples.

Compliance with ethical standards

References

Ahmadpour A, Asl AH, Fallah N (2018) Synthesis and photocatalytic studies of TiO_2-clinoptilolite on spent caustic wastewater treatment. Particul Sci Technol 36(7):791–798. https://doi.org/10.1080/02726351.2017.1302534

Aman N, Satapathy PK, Mishra T, Mahato M, Das NN (2012) Synthesis and photocatalytic activity of mesoporous cerium doped TiO_2 as visible light sensitive photocatalyst. Mater Res Bull 47(2):179–183. https://doi.org/10.1016/j.materresbull.2011.11.049

Anastas PT, Kirchhoff MM (2002) Origins, current status, and future challenges of green chemistry. ACC Chem Res 35(9):686–694. https://doi.org/10.1021/ar010065m

Arellano U, Wang JA, Asomoza M, Chen LF, González J, Manzo A, Solis S, Lara VH (2018) Crystalline structure, surface chemistry and catalytic properties of Fe^{3+} doped TiO_2 sol–gel catalysts for photooxidation of 2,4–dichlorophenoxyacetic acid. Mater Chem Phys 214:247–259. https://doi.org/10.1016/j.matchemphys.2018.04.093

Baláž P (2008) Mechanochemistry in Nanoscience and Minerals Engineering. Springer-Verlag, Berlin

Banisharif A, Khodadadi AA, Mortazavi Y, Anaraki Firooz A, Beheshtian J, Agah S, Menbari S (2015) Highly active Fe_2O_3-doped TiO_2 photocatalyst for degradation of trichloroethylene in air under UV and visible light irradiation: Experimental and computational studies. Appl Catal B Environ 165:209–221. https://doi.org/10.1016/j.apcatb.2014.10.023

Baoum A, Amin MS, Mohamed RM (2019) Development of $CuCr_2O_4$ nanocomposite adopting decoration with polyaniline for acridine orange dye degradation. Appl Nanosci. https://doi.org/10.1007/s13204-019-01218-8

Bhachu DS, Sathasivam S, Carmalt CJ, Parkin IP (2014) PbO-Modified TiO_2 thin films: a route to visible light photocatalysts. Langmuir 30(2):624–630. https://doi.org/10.1021/la4038777

Buda W, Czech B (2013) Preparation and characterization of C, N-codoped TiO_2 photocatalyst for the degradation of diclofenac from wastewater. Water Sci Technol 68(6):1322–1328. https://doi.org/10.2166/wst.2013.369

Charmas B, Kucio K, Sydorchuk V, Khalameida S, Zięzio M, Nowicka A (2019) Characterization of multimodal silicas using TG/DTG/DTA, Q-TG, and DSC methods. Colloids Interfaces 3(1):6. https://doi.org/10.3390/colloids3010006

Charmas B, Skubiszewska-Zięba J, Waniak-Nowicka H (2017) Thermal and calorimetric investigations oftitania–silica composites. Adsorpt Sci Technol 235:706–713. https://doi.org/10.1177/0263617417706796

Chibac AL, Buruiana T, Melinte V, Buruiana EC (2017) Photocatalysis applications of some hybrid polymeric composites incorporating TiO_2 nanoparticles and their combinations with SiO_2/Fe_2O_3. Beilstein J Nanotech 8:272–286. https://doi.org/10.3762/bjnano.8.30

Cho S, Choi W (2001) Solid-phase photocatalytic degradation of PVC–TiO_2 polymer composites. J Photoch Photobio A 143(2–3):221–228. https://doi.org/10.1016/S1010-6030(01)00499-3

Daghrir R, Drogui P, Robert D (2013) Modified TiO_2 for environmental photocatalytic applications: a review. Ind Eng Chem Res 52(10):3581–3599. https://doi.org/10.1021/ie303468t

Di Valentin C, Pacchioni G, Selloni A (2004) Origin of the different photoactivity of N-doped anatase and rutile TiO_2. Phys Rev B 70(8):085116. https://doi.org/10.1103/PhysRevB.70.085116

Ganesh I, Kumar PP, Gupta AK, Sekhar PSC, Radha K, Padmanabham G, Sundararajan G (2012) Preparation and characterization of Fe-doped TiO_2 powders for solar light response and photocatalytic applications. Process Appl Ceram 6(1):21–36. https://doi.org/10.2298/pac1201021g

Grabowska E, Zaleska A, Sobczak JW, Gazda HJ (2009) Boron-doped TiO_2: Characteristics and photoactivity under visible light. Procedia Chem 1(2):1553–1559. https://doi.org/10.1016/j.proche.2009.11.003

Gregg SJ, Sing KSW (1982) Adsorption, Surface Area and Porosity, second edition. Academic Press, London

Gun'ko VM (2014) Composite materials: Textural characteristics. Appl Surf Sci 307:444–454. https://doi.org/10.1016/j.apsusc.2014.04.055

Gun'ko VM, Do DD (2001) Characterization of pore structure of carbon adsorbents using regularization procedure. Coll Surf A 19:71–83

Gun'ko Mikhalovsky VMSV (2004) Evaluation of slitlike porosity of carbon adsorbents. Carbon 42:843–849. https://doi.org/10.1016/j.carbon.2004.01.059

Hirai T, Suzuki K, Komasawa I (2001) Preparation and photocatalytic properties of composite cds nanoparticles-titanium dioxide particles. J Colloid Interface Sci 244(2):262–265. https://doi.org/10.1006/jcis.2001.7982

Ho W, Yu JC, Lee S (2006) Low-temperature hydrothermal synthesis of S-doped TiO_2 with visible light photocatalytic activity. J Solid State Chem 179(4):1171–1176. https://doi.org/10.1016/j.jssc.2006.01.009

Inturi SNR, Boningari T, Suidan M, Smirniotis PG (2014) Visible-light-induced photodegradation of gas phase acetonitrile using aerosol-made transition metal (V, Cr, Fe Co, Mn, Mo, Ni, Cu, Y, Ce, and Zr) doped TiO2. Appl Catal B Environ 144:333–342. https://doi.org/10.1016/j.apcatb.2013.07.032

Jraba A, Anna Z, Elaloui E (2019) Effects of Sr^{2+}, Fe^{3+} and Al^{3+} doping on the properties of TiO_2 prepared using the sol-gel method. C R Chim 22:9–10. https://doi.org/10.1016/j.crci.2019.10.003

Julkapli NM, Bagheri S, Abd Hamid SB (2014) Recent advances in heterogeneous photocatalytic decolorization of synthetic dyes. Sci World J. https://doi.org/10.1155/2014/692307

Khaki MRD, Shafeeyan MS, Raman AAA, Daud WMAW (2018) Evaluating the efficiency of nano-sized Cu doped TiO_2/ZnO photocatalyst under visible light irradiation. J Mol Liq 258:354–365. https://doi.org/10.1016/j.molliq.2017.11.030

Kim DH, Choi DK, Kim SJ, Lee KS (2008) The effect of phase type on photocatalytic activity in transition metal doped TiO_2 nanoparticles. Catal Commun 9(5):654–657. https://doi.org/10.1016/j.catcom.2007.07.017

Kokorin AI, Amal R, Teoh WY, Kulak AI (2017) Studies of nano-sized iron-doped tio_2 photocatalysts by spectroscopic methods. Appl Magn Reson 48(5):447–459. https://doi.org/10.1007/s00723-017-0873-1

Kong LB, Huang JMH, Zhang RF (2002) Effect of excess PbO on microstructure and electrical properties of PLZT7/60/40 ceramics derived from a high-energy ball milling process. J Alloys Compd 345:238–245. https://doi.org/10.1016/S0925-8388(02)00400-0

Kucio K, Charmas B, Pasieczna-Patkowska S (2019) Structural, thermal and photocatalytic properties of composite materials $SiO_2/TiO_2/C$. Adsorption 25(3):501–511. https://doi.org/10.1007/s10450-019-00032-6

Kumar MRA, Abebe B, Nagaswarupa HP, Murthy HCA, Ravikumar CR, Sabir FK (2020) Enhanced photocatalytic and electrochemical performance of TiO_2-Fe_2O_3 nanocomposite: Its applications in dye decolorization and as supercapacitors. Sci Rep. https://doi.org/10.1038/s41598-020-58110-7

Kumar SG, Devi LG (2011) Review on modified TiO_2 photocatalysis under UV/visible light: selected results and related mechanisms on interfacial charge carrier transfer dynamics. J Phys Chem A 115(46):13211–13241. https://doi.org/10.1021/jp204364a

Leboda R, Mendyk E (1982) Thermal modification of silica gels with temperature programing. J Therm Anal 25(2):449–462. https://doi.org/10.1007/bf01912971

Leong S, Razmjou A, Wang K, Hapgood K, Zhang X, Wang H (2014) TiO$_2$ based photocatalytic membranes: A review. J Membrane Sci 472:167–184. https://doi.org/10.1016/j.memsci.2014.08.016

Liu G, Chen Z, Dong C, Zhao Y, Li F, Lu GQ, Cheng HM (2006) Visible light photocatalyst: iodine-doped mesoporous titania with a bicrystalline framework. J Phys Chem B 110(42):20823 20828. https://doi.org/10.1021/jp062946m

Miao J, Zhang R, Zhang L (2018) Photocatalytic degradations of three dyes with different chemical structures using ball-milled TiO$_2$. Mat Res Bull 97:109–114. https://doi.org/10.1016/j.materresbull.2017.08.032

Mohamed RM, Baeissa ES, Mkhalid IA, Al-Rayyani MA (2013) Optimization of preparation conditions of ZnO-SiO$_2$ xerogel by sol-gel technique for photodegradation of methylene blue dye. Appl Nanosci 3(1):57–63. https://doi.org/10.1007/s13204-012-0074-z

Molchanov VV, Buyanov RA (2001) Scientific grounds for the application of mechanochemistry to catalyst preparation. Kinet Catal 42(3):366–374. https://doi.org/10.1023/A:1010465315877

Moniz SJA, Shevlin SA, An X, Guo ZX, Tang J (2014) Fe$_2$O$_3$-TiO$_2$ Nanocomposites for enhanced charge separation and photocatalytic activity. Chem Eur 20(47):15571–15579. https://doi.org/10.1002/chem.201403489

Pirkanniemi K, Sillanpää M (2002) Heterogeneous water phase catalysis as an environmental application: a review. Chemosphere 48(10):1047–1060. https://doi.org/10.1016/S0045-6535(02)00168-6

Rouquerol J, Baron G, Denoyel R, Giesche H, Groen J, Klobes P, Levitz P, Neimark AV, Rigby S, Skudas R, Sing K, Thommes M, Unger K (1994) Recommendations for the characterization of porous solids. Pure Appl Chem 66:1739–1758

Rožić L, Petrović S, Lončarević D, Grbić B, Radić N, Stojadinović S, Jović V, Lamovec J (2019) Influence of annealing temperature on structural, optical and photocatalytic properties of TiO$_2$-CeO$_2$ nanopowders. Ceram Int 45(2):2361–2367. https://doi.org/10.1016/j.ceramint.2018.10.153

Santhi K, Manikandan P, Rani C, Karuppuchamy S (2015) Synthesis of nanocrystalline titanium dioxide for photodegradation treatment of remazol brown dye. Appl Nanosci 5(3):373–378. https://doi.org/10.1007/s13204-014-0327-0

Saqlain S, Cha BJ, Kim SY, Ahn TK, Park C, Oh JM, Jeong EC, Seo HO, Kim YD (2020) Visiblelight-responsive Fe-loaded TiO$_2$ photocatalysts for totaloxidation of acetaldehyde: Fundamentalstudiestowardslarge-scaleproduction and applications. Appl Surf Sci 505:144–160. https://doi.org/10.1016/j.apsusc.2019.144160

Shojaei FA, Shams-Nateri A, Ghomashpasand M (2015) Comparative study of photocatalytic activities of magnetically separable WO$_3$/TiO$_2$/Fe$_3$O$_4$ nanocomposites and TiO$_2$, WO$_3$/TiO$_2$ and TiO$_2$/Fe$_3$O$_4$ under visible light irradiation. Superlattice Microst 88:211–224. https://doi.org/10.1016/j.spmi.2015.09.014

Silva AMT, Silva CG, Dražić G, Faria JL (2009) Ce-doped TiO$_2$ for photocatalytic degradation of chlorophenol. Catal Today 144(1–2):13–18. https://doi.org/10.1016/j.cattod.2009.02.022

Sin JC, Lam SM, Mohamed AR, Lee KT (2012) Degrading Endocrine Disrupting Chemicals from Wastewater by TiO$_2$ Photocatalysis: A Review. Int J Photoenergy. https://doi.org/10.1155/2012/185159

Skubiszewska-Zięba J, Charmas B, Leboda R, Tertykh VA, Yanishpolskii VV (2012) Complex investigations of structural and thermal properties of silica-titania adsorbents. J Therm Anal Calorim 108(3):1085–1092. https://doi.org/10.1007/s10973-011-1943-5

Subramonian W, Wu TY, Chai SP (2017) Photocatalytic degradation of industrial pulp and paper mill effluent using synthesized magnetic Fe$_2$O$_3$-TiO$_2$: Treatment efficiency and characterizations of reused photocatalyst. J Environ Manage 187:298–310. https://doi.org/10.1016/j.jenvman.2016.10.024

Suryanarayana C (2001) Mechanical alloying and milling. Prog Materials Sci 46(1–2):1–184. https://doi.org/10.1016/S0079-6425(99)00010-9

Thakur V, Kushwaha HS, Singh A, Vaish R, Punia R, Singh L (2015) A study on the structural and photocatalytic degradation of ciprofloxacine using (70B$_2$O$_3$-29Bi$_2$O$_3$-1Dy$_2$O$_3$)- x(BaO-TiO$_2$) glass ceramics. J Non-Cryst Solids 428:197–203. https://doi.org/10.1016/j.jnoncrysol.2015.08.009

Trapalis CC, Keivanidis P, Kordas G, Zaharescu M, Crisan M, Szatvanyi A, Gartner M (2003) TiO$_2$ (Fe^{3+}) nanostructured thin films with antibacterial properties. Thin Solid Films 433(1–2):186–190. https://doi.org/10.1016/S0040-6090(03)00331-6

Wang Y, Fan X, Wang S, Zhang G, Zhang F (2013) Magnetically separable γ-Fe$_2$O$_3$/TiO$_2$ nanotubes for photodegradation of aqueous methyl orange. Mater Res Bull 48(2):785–789. https://doi.org/10.1016/j.materresbull.2012.11.058

Wu X, Su P, Liu H, Qi L (2009) Photocatalytic degradation of Rhodamine B under visible light with Nd-doped titanium dioxide films. J Rare Earths 27(5):739–743. https://doi.org/10.1016/S1002-0721(08)60326-9

Yao S, Sui C, Shi Z (2011) Preparation and characterization of visible-light-driven europium doped mesoporous titania photocatalyst. J Rare Earth 29(10):929–933. https://doi.org/10.1016/S1002-0721(10)60571-6

Zaleska A (2008) Doped-TiO$_2$: a review. Recent Patents Eng 2(3):157–164. https://doi.org/10.2174/187221208786306289

Zhang J, Zhou P, Liu J, Yu J (2014) New understanding of the difference of photocatalytic activity among anatase, rutile and brookite TiO$_2$. Phys Chem Chem Phys 16(38):20382–20386. https://doi.org/10.1039/c4cp02201g